PCCP

ROYAL SOCIETY OF CHEMISTRY

PAPER

View Article Online
View Journal | View Issue

Cite this: *Phys. Chem. Chem. Phys.*, 2026, **28**, 234

Azurin-based peptide p28 disrupts p53–HDM2 interactions: insights from *in silico* studies

Albin Joy, [a] Anand Srivastava [b] and Rajib Biswas *[c]

This study investigates the potential anticancer activity of the azurin-derived peptide p28 through its molecular interactions with human double minute 2 (HDM2), a key negative regulator of the tumor suppressor protein p53. By binding to the p53 transactivation domain, HDM2 impairs p53's tumor-suppressive functions. Using the information-driven docking platform HADDOCK, we generated ten plausible binding poses of p28 with the HDM2 N-terminal domain. Each pose was subsequently refined *via* three independent 300 ns all-atom molecular dynamics simulations, resulting in a cumulative 9 μs trajectory. Although this workflow does not capture spontaneous binding or pose interconversion, it enables systematic refinement and stability assessment of docking-generated complexes. From this analysis, three stable conformations (D3, D4, and D5) have emerged, consistently occupying the HDM2 hydrophobic pocket and exhibiting favorable binding energies (MMPBSA). Residue-level interaction analysis revealed that p28 engages HDM2 hotspots important for p53 recognition, suggesting a competitive mode of binding. While experimental studies and enhanced sampling simulations are required to fully validate these findings, our results provide a refined structural basis for understanding how p28 may interfere with HDM2–p53 interactions and support its promise as a peptide-based anticancer candidate.

Received 20th June 2025,
Accepted 13th November 2025

DOI: 10.1039/d5cp02358k

rsc.li/pccp

1 Introduction

Human double minute 2 (HDM2), the human homologue of the originally identified mouse double minute 2 (MDM2), is a 491-amino acid phosphoprotein that plays a critical role in regulating the p53 tumour suppressor protein.[1] The p53 tumour suppressor is a pivotal regulator of cellular stress responses, playing a crucial role in enforcing cell growth arrest, inducing senescence, and initiating apoptosis in response to various forms of cellular stress.[2,3] Its ability to suppress the propagation of cells harbouring damaged or potentially mutagenic DNA is vital for maintaining genomic integrity. The p53 protein mediates these protective effects primarily through a transcription-dependent mechanism.[4,5] A central feature of p53 biology is its tight regulation at the protein level, as cellular p53 concentrations are a key determinant of its function. In unstressed cells, p53 is maintained at low levels due to its rapid degradation, with a half-life of 5 to 30 minutes, primarily controlled by the ubiquitin ligase MDM2.[2,3] Upon exposure to stress, p53 levels are swiftly elevated, allowing it to exert its tumour suppressor functions effectively.

Structural studies of the p53–MDM2 complex reveal that MDM2's amino-terminal domain binds to p53's transactivation domain (TAD) within a hydrophobic pocket.[6] This interaction involves residues 25–109 of MDM2 forming the HDM2 NTD and a 15-amino acid amphipathic peptide of p53, with key binding sites located at residues 18–26 of p53.[7–9] Residues PHE19, TRP23, and LEU26 of p53, which bind to the hydrophobic pocket of HDM2, play a crucial role in this protein–protein interaction. This interaction is essential for the regulation of p53's tumour suppressor activity, as HDM2 binding leads to its functional inhibition.[7,10] The interaction is characterised by a precise key-lock fit, with p53's amphipathic α-helix fitting into a hydrophobic cleft in MDM2. THR18 in p53 stabilises this α-helix, while MDM2's binding cleft, formed by residues 54–74 and 94–104, features a groove lined with hydrophobic and aromatic residues. Conversely, mutations at GLY58, GLU68, VAL75, or CYS77 in MDM2 can disrupt its binding to p53.[11] Fig. 1 illustrates the native HDM2–p53 interaction sites, highlighting the hydrophobic cleft and the crucial binding residues of p53. The binding affinity of the p53–MDM2 complex ranges from 60 to 700 nM, depending on the number of residues of the p53 protein involved.[12–14] Such binding inhibits p53's ability to activate transcription by physically blocking its interaction with the transcriptional machinery.

[a] *Department of Chemistry, Indian Institute of Technology Tirupati, Yerpedu, Tirupati, Andhra Pradesh 517619, India*
[b] *Molecular Biophysics Unit, Indian Institute of Science, Bangalore, Karnataka 560012, India*
[c] *Department of Chemistry, Indian Institute of Technology Tirupati, Yerpedu, Tirupati, Andhra Pradesh 517619, India. E-mail: rajib@iittp.ac.in*

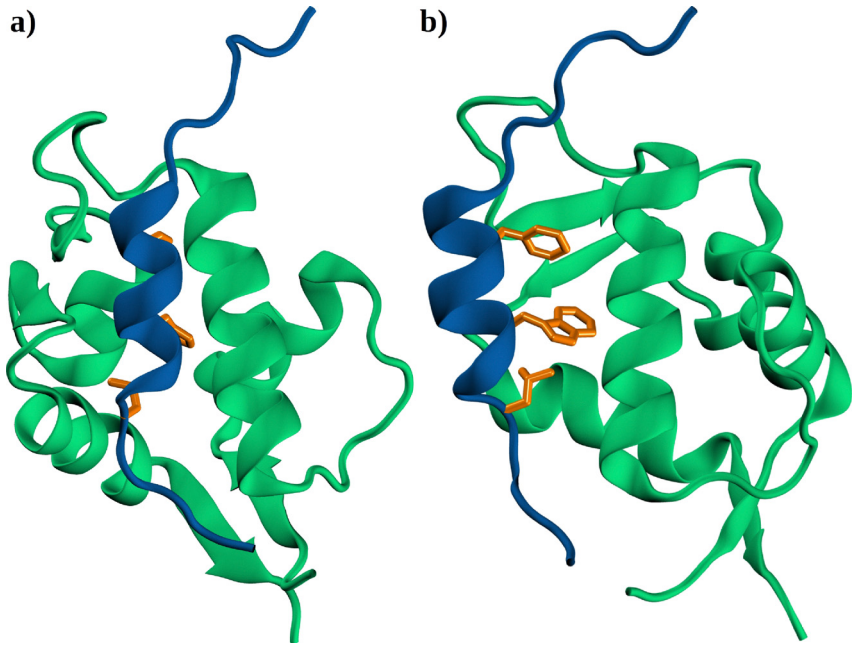

Fig. 1 (a) Cartoon representation of the native HDM2–p53 interaction sites and the hydrophobic cleft. p53 (residues 10–30) is coloured blue and HDM2 (residues 25–111) in green. (b) Residues PHE19, TRP23, and LEU26 of p53, represented in stick model and coloured orange, bind to the hydrophobic pocket of HDM2.

As an E3 ubiquitin ligase, MDM2 is primarily responsible for tagging p53 for degradation, thus controlling its cellular levels.[15,16] MDM2 features a self- and p53-specific ubiquitin ligase activity, which is essential for its function. This is responsible for transferring ubiquitin to lysine residues in the COOH terminus of p53, marking it for degradation. MDM2 and p53 regulate each other through an autoregulatory feedback loop, which is essential for cellular homeostasis and effective response to various cellular stresses.[7,17,18] p53 induces the expression of MDM2, which in turn inhibits p53 by promoting its degradation and nuclear export. This feedback mechanism ensures that p53 activity is tightly controlled. Also, various DNA-damaging agents and oncogenes can activate p53, leading to disruption of p53–MDM2 interactions and stabilization of p53, thereby allowing it to perform its tumour-suppressive functions.

Due to the well-characterised structural and biological nature of the hydrophobic interaction between p53 and MDM2, designing small lipophilic molecules that disrupt or inhibit this interaction has become a promising therapeutic approach. Notably, the MDM2 protein presents structurally well-defined binding sites, whereas p53 undergoes dynamic conformational changes. This suggests that inhibitors should more closely imitate p53 rather than MDM2. Additionally, only the p53 protein interface has a single short contiguous stretch of residues, making it a suitable model for designing small peptide inhibitors. The interaction between p53 and MDM2 involves only three hydrogen bonds, with the most critical bond being formed by TRP23 on p53.[6–9] The relatively small contact surface between these two proteins further supports the idea that small inhibitory peptides or molecules could effectively disrupt their interaction.

A recent study, recognised with the Nobel Prize in Chemistry 2024, focuses on the design of high-affinity competitive inhibitors through *in silico* approaches that scaffold the p53 helix and establish additional interactions with MDM2.[19] They utilised deep learning techniques to effectively scaffold protein functional sites and demonstrated promising results. Furthermore, an enhanced deep learning-based generative model for protein backbones, called RFdiffusion, was used for enzyme active site scaffolding in the MDM2–p53 binding interaction.[20] This model generated 96 scaffold designs for the helical region of p53 in the presence of MDM2, which were further characterised experimentally.

Previous studies have suggested that azurin and its derived peptides possess significant anticancer properties, demonstrating the ability to inhibit the growth and proliferation of various cancer cell types.[21–23] Some works have shown that the p28 peptide (a small peptide derived from azurin having residues LEU50–ASP77 of azurin) can stabilise the p53 tumour suppressor protein, preventing its degradation and thereby arresting cancer cell growth.[24,25] By binding to the DNA-binding domain (DBD) of p53, p28 effectively shields it from cellular mechanisms that lead to its degradation.[26–29] Another study has shown that the binding of azurin to p53 significantly decreases the association rate constant and binding affinity between MDM2 and p53, without blocking MDM2's access to p53's binding pocket.[30]

Building on these findings, our study aims to investigate the molecular interactions between the azurin-based peptide p28 and the cancer-related protein HDM2. Specifically, we seek to uncover the mechanisms by which azurin exerts its anticancer effects, particularly through disrupting the HDM2–p53

interaction, a critical pathway in tumour suppression. By focusing on the binding affinity and conformational dynamics of these complexes, we provide deeper insights into the therapeutic potential of p28 as a promising peptide-based anticancer agent, contributing to the development of novel treatments targeting HDM2-associated cancers.

2 Methods

As mentioned earlier, HDM2 acts as a downregulator of p53 by binding to its transactivation domain (TAD), which diminishes its tumour-suppressive function. In this study, we investigate the interaction between the p28 peptide and the N-terminal domain (NTD) of HDM2, the region responsible for binding to the TAD of p53, which leads to p53 inhibition. Our approach includes protein docking studies, molecular dynamics simulations, and energy calculations to evaluate the binding affinity and stability of the HDM2–p28 complex.

2.1 Docking of HDM2 and the p28 peptide

We used the N-terminal domain (NTD) of HDM2 (amino acids 25–111) with a resolution of 1.8 Å obtained from the RCSB Protein Data Bank (PDB ID: 6Q96) and extracted the p28 peptide fragment (amino acids 50–77) from the azurin structure (PDB ID: 4AZU).[31,32] No terminal capping was applied; the peptide termini were modelled in their standard charged forms (NH_3^+ at the N-terminus and COO^- at the C-terminus). HIS73 and HIS96 in HDM2 were modelled in the HIE tautomeric state (protonation on Nε2). The ligand present in the HDM2 crystal structure (PDB ID: 6Q96) was removed using VMD. The HDM2 protein was then placed in a cubic box with a minimum distance of 1.2 nm from the box edge. The system was subjected to energy minimization using the steepest descent algorithm until the maximum force was less than 1000 kJ mol^{-1} nm^{-1}. Subsequently, equilibration was performed in the NVT ensemble for 10 ns, followed by NPT simulations at 1 bar and 300 K for 100 ns. The same equilibration and simulation protocol was applied to the p28 peptide system. The major α-helical secondary structure of p28 was found to remain stable during the 100 ns equilibration in explicit solvent. The final equilibrated structures of the HDM2 NTD and the p28 peptide were then used for docking studies. Docking was performed using the HADDOCK (High Ambiguity Driven protein–protein DOCKing) server, which generated the top 10 most reliable clusters based on energy scores.[33,34]

The HADDOCK docking process starts with randomizing the orientations and performing rigid-body minimisation of the interacting partners, such as the p28 peptide and the HDM2 NTD. These molecules are treated as rigid bodies, with fixed geometrical parameters, and are randomly rotated to explore possible configurations. Next, a rigid-body energy minimisation step is performed, optimizing the interaction by identifying low-energy conformations. In the next stage, flexibility is introduced through molecular dynamics-based refinement, initially optimizing orientations, followed by applying flexibility to the interface atoms (within 5 Å) and relaxing side chains. Finally, the complex undergoes a brief MD simulation at 300 K in a solvent shell, gradually relaxing position restraints to optimise interactions.

HADDOCK employs a scoring system based on a combination of factors, including van der Waals forces, electrostatics, desolvation energies, and empirical restraints derived from experimental data or predictions. In our analysis, the server generated a set of docking models, grouped into clusters based on similarity. The top 10 clusters generated are ranked according to their HADDOCK and *Z*-scores, reflecting the reliability and quality of each predicted binding mode.

2.2 MD simulations of docked structures

Each of these structures was placed in a simulation box at a distance of 1.2 nm from the box walls and solvated with water. The docked complex has a net charge of +1, which was neutralized by adding one Cl^- ion. Additional Na^+ and Cl^- ions were introduced to maintain a physiological salt concentration of 0.15 M. All systems have a final molarity of approximately 0.15 M. We employed the CHARMM36m force field parameters for the protein chains and the TIP3P model for water molecules. Molecular dynamics simulations were carried out using the GROMACS software suite.[35]

Energy minimisation was performed using the steepest descent method to resolve steric clashes, achieving convergence once the forces reached below 1000 kJ mol^{-1} nm^{-1}. The energy-minimised structure was then equilibrated at 300 K in the NVT ensemble for 1 ns, followed by pressure equilibration at 1 bar in the NPT ensemble for 1 ns. The equilibrated system was then subjected to a production run in the NVT ensemble for 300 ns, with data collected every picosecond. Temperature and pressure were maintained at 300 K and 1 bar, respectively, using a Nosé–Hoover thermostat[36,37] with a relaxation time of 0.5 ps and a Parrinello–Rahman barostat[38,39] with a relaxation time of 1.0 ps. We examined the stability and pressure behaviour of the NVT simulations for a set of ten structures, and the corresponding results are provided in the SI. All systems exhibited stable trajectories throughout the simulations, indicating well-equilibrated configurations. Electrostatic parameters were calculated using the particle-mesh Ewald (PME) method[40] with a real-space cutoff of 1.0 nm, a Fourier grid spacing of 0.14 nm, an interpolation order of 4, and a tolerance of 1×10^{-5}. All van der Waals interactions were truncated at a 1.0 nm cut-off, with the neighbour list updated every ten steps. The LINCS (LINear Constraint Solver) algorithm[41] was used to constrain the bond lengths of hydrogen atoms.

We carried out 3 sets of simulations with different initial velocities for each of the 10 docked structures, resulting in a cumulative 9 μs molecular dynamics trajectory. The trajectory was analysed to evaluate the sustained interactions between HDM2 and p28. We found 3 structures that adapt different binding poses and in which the p28 peptide effectively binds and masks the binding pocket on the HDM2 protein.

2.3 Subsequent docking studies with the p53 TAD

The final structures of the above 3 clusters were subjected to a second docking study involving the p53 TAD (residues 10–30)

obtained from the human p53 structure in the UniProt database (ID: P04637). This docking was performed to study the binding of the p53 TAD to the HDM2–p28 complex. The top clusters from these docking studies were analysed to understand how the presence of the p28 peptide influences the binding modes of HDM2 with the p53 TAD.

3 Results and discussion

3.1 HADDOCK scores of p28 docking to HDM2

The docking of the p28 peptide with the N-terminal domain (NTD) of HDM2 yielded a total of 10 distinct cluster structures, highlighting various potential binding modes. In the rest of this article, we refer to these structures as D1, D2, . . ., D10. The best models from these top 10 HADDOCK clusters are presented in Fig. 2. Interestingly, in many of these docked complexes, the p28 peptide was found to bind near the region of the hydrophobic pocket of the HDM2 NTD. This hydrophobic pocket of HDM2 is known for its interaction with the transactivation domain (TAD) of the p53 tumour suppressor protein, suggesting that p28 may potentially interfere with or mimic this critical binding interface. (Native HDM2–p53 interaction sites and the hydrophobic cleft are depicted in Fig. 1.) These structures are ranked by the HADDOCK server based on the HADDOCK scores (obtained using eqn (1)), which quantify the overall docking energy as a weighted sum of various interaction energy terms, and are presented in Table 1. The HADDOCK score is computed using the following weighted energy equation:

$$\text{HADDOCK score} = 1E_{\text{vdW}} + 0.2E_{\text{elec}} + 1E_{\text{desolv}} + 0.1E_{\text{AIR}} \quad (1)$$

3.2 Structural stability of HDM2–p28 complexes

These structures were subjected to MD simulations at 300 K for 300 ns to assess the stability of the interactions and to

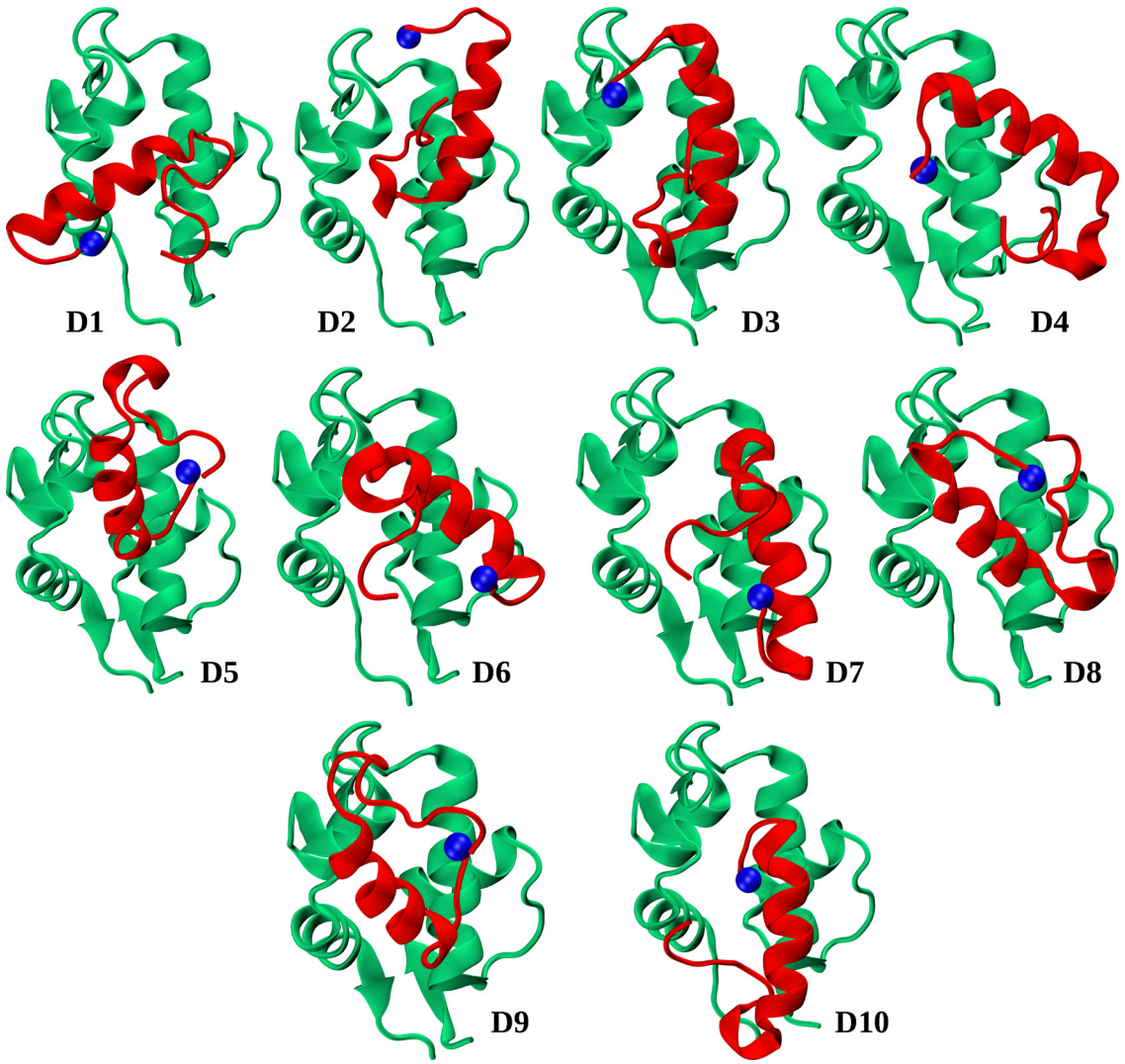

Fig. 2 Cartoon representation of the docked complexes D1 to D10 obtained from the HADDOCK server showing different binding poses of the p28 peptide with the HDM2 NTD. The HDM2 protein is coloured green and the p28 peptide is shown in red. The N-terminal nitrogen atom of the p28 peptide is depicted as a blue sphere.

Table 1 Details of the clusters generated from the HADDOCK server for HDM2–p28 docking

Complex	HADDOCK score
D1	−77.6 ± 11.0
D2	−71.5 ± 7.5
D3	−68.7 ± 2.0
D4	−64.9 ± 5.5
D5	−64.0 ± 9.2
D6	−61.9 ± 6.2
D7	−58.3 ± 8.0
D8	−58.0 ± 5.6
D9	−57.8 ± 8.6
D10	−55.3 ± 4.6

accommodate any conformational changes leading to the most favourable low-energy binding interactions. We checked the convergence of the docking interactions by calculating the RMSD of the p28 backbone atoms and the SASA of the hydrophobic pocket of the HDM2 NTD using the last 200 ns of simulation data. These results, depicted in Fig. 3, demonstrate convergence and sustained interactions of the p28 peptide with HDM2. Consistent trends were observed across the three independent replicas, further supporting the convergence and reproducibility of the binding interactions. These MD trajectories of the different equilibrated structures were further analysed to evaluate the stability of various binding poses, sustained interactions and structural behaviour of the protein chains.

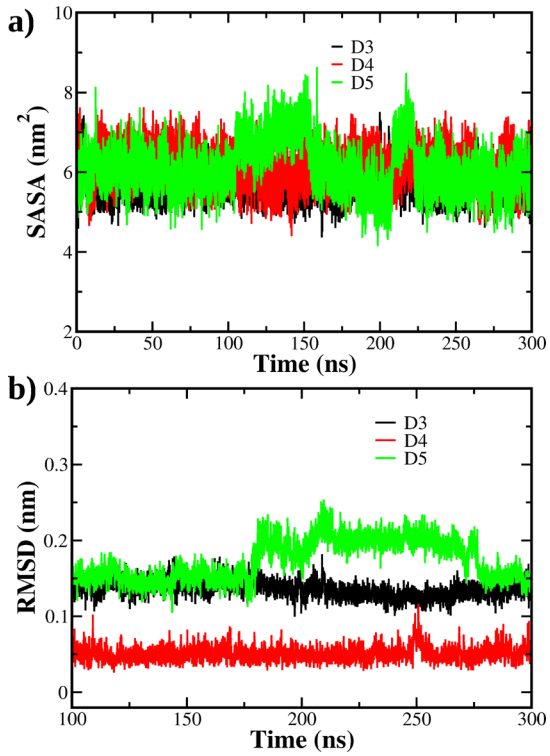

Fig. 3 (a) Temporal evolution of the solvent-accessible surface area (SASA) of the HDM2 hydrophobic pocket and (b) RMSD of the p28 peptide backbone during the MD simulations.

First, the distance between the centre of mass (COM) of the HDM2 hydrophobic pocket and the p28 peptide was calculated to determine whether the p28 peptide continuously interacts with HDM2 throughout the simulations, which is depicted in Fig. 4. In general, we found that p28 consistently interacted with HDM2 in all 10 structures, maintaining proximity throughout the simulation. However, in a few sets of simulations for D1, D6, D7, and D8, the peptide did not bind to the hydrophobic pocket. Next, we assessed the temporal evolution of the root mean square deviation (RMSD) of backbone atoms and the radius of gyration (R_g) for both protein chains (depicted in Fig. 5). The HDM2 NTD exhibited minimal deviations compared to the initial structure, indicating overall structural stability. The p28 peptide, on the other hand, mostly retained its folded α-helical structure, although slight structural melting was observed in a few cases. We further calculated the solvent accessible surface area (SASA) of the residues forming the hydrophobic pocket of HDM2 to identify which structures had the HDM2 binding site masked by p28. Among all the trajectories, the D4, D5, and D10 complexes showed relatively lower SASA values for the hydrophobic pocket of HDM2, indicating more extensive masking of the hydrophobic pocket by p28 in this model. These analyses are shown in Fig. 5.

Next, we analysed the root mean square fluctuations (RMSF) of Cα carbon atoms (Cα-RMSF) for individual residues in both protein chains over the last 50 ns of the three sets of MD trajectories. These are depicted in Fig. 6. The analysis showed that most of the residues of HDM2 remained structurally rigid, closely resembling their native states under the simulated conditions. The p28 peptide exhibits slightly greater fluctuations, as expected, reflecting its considerable structural flexibility. This flexibility may contribute to its ability to adapt to various conformational states, allowing for dynamic interactions with HDM2. In general, residues 5–25 of p28 remain relatively stable in their native α-helical structure, probably with their interactions with HDM2. The N- and C-terminal residues exhibited higher fluctuations.

3.3 Conformational diversity of the HDM2–p28 complexes

After the 300 ns simulation, several docked complexes converged to similar binding modes. Three pairs of such similar complexes were identified: D2–D6, D4–D10, and D5–D9. Upon analysing the binding regions in the final structures, we observed that in D1 and D2, the p28 peptide binds near the active region of HDM2. However, for D1, the binding modes differ across the three sets of trajectories. Similarly, for D6, D7, and D8, in certain trajectories, the p28 peptide moved away from the active site. In D4, the N-terminal end of p28, with its hydrophobic leucine residue, interacts with the hydrophobic pocket of HDM2. This binding pattern is also seen in D10. In D5 and D9, p28 aligns perfectly within the hydrophobic groove. Now, from these 10 complexes, we narrowed the selection to three conformationally relevant structures that effectively block the hydrophobic pocket, display structurally unique binding patterns, maintain sustained interchain interactions, and exhibit favourable binding energies. These are complexes D3, D4, and D5, which are further studied

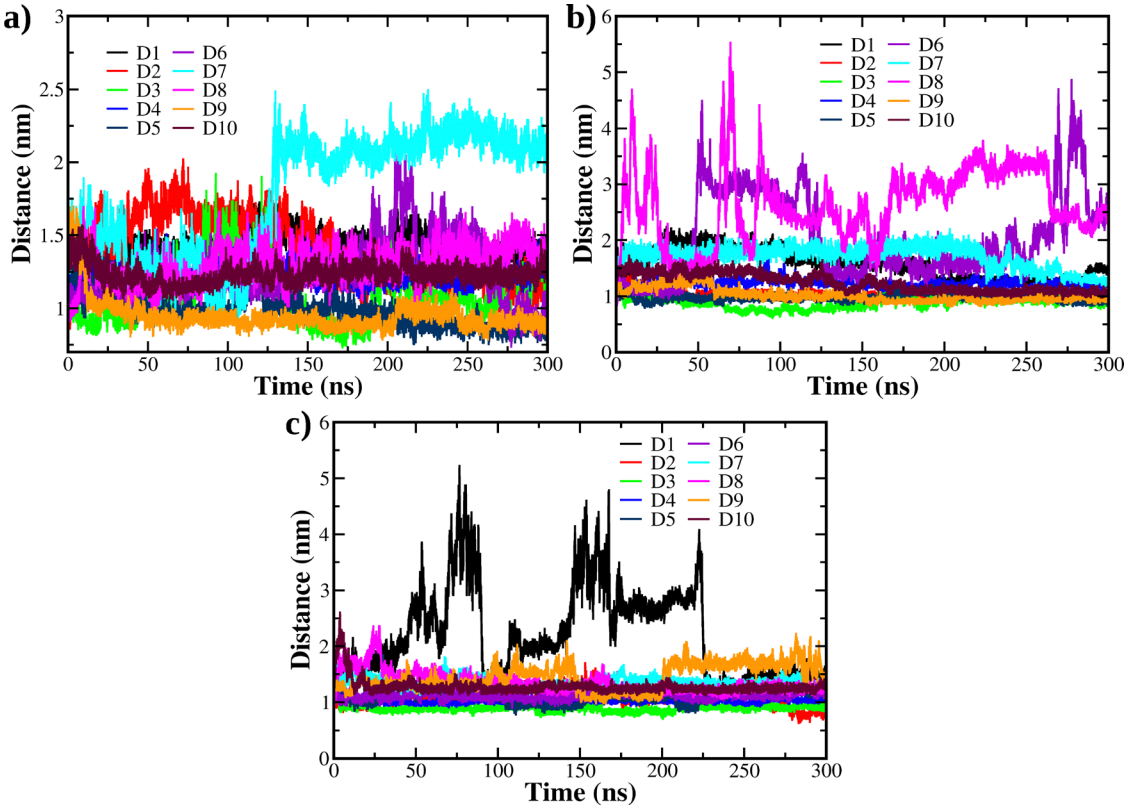

Fig. 4 (a)–(c) Temporal evolution of the distance between the centre of mass (COM) of the HDM2 hydrophobic pocket and the p28 peptide across the top 10 docked models generated by the HADDOCK server for the three sets of simulations started with different initial velocities.

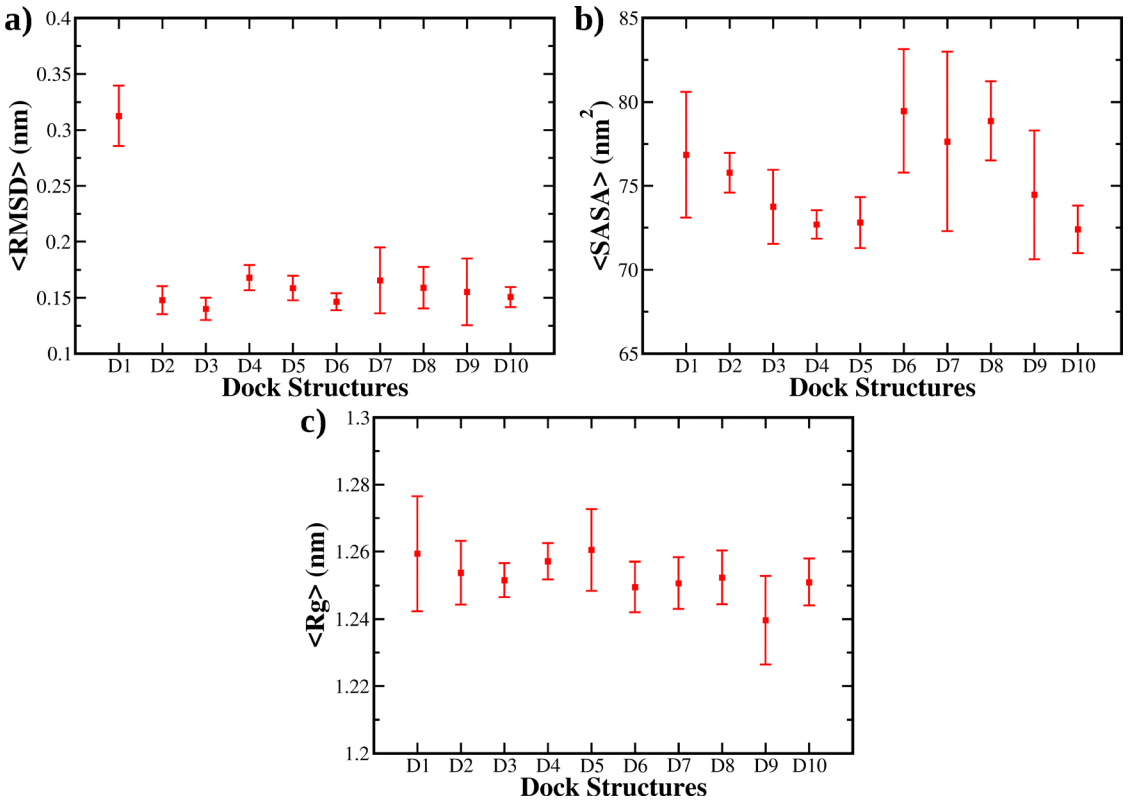

Fig. 5 The average of (a) root mean square deviation (RMSD) of backbone atoms, (b) solvent accessible surface area (SASA) of the hydrophobic pocket, and (c) radius of gyration (R_g) of backbone atoms of the HDM2 NTD for the 10 docked models (D1, D2, …, D10), calculated over the three sets of trajectories.

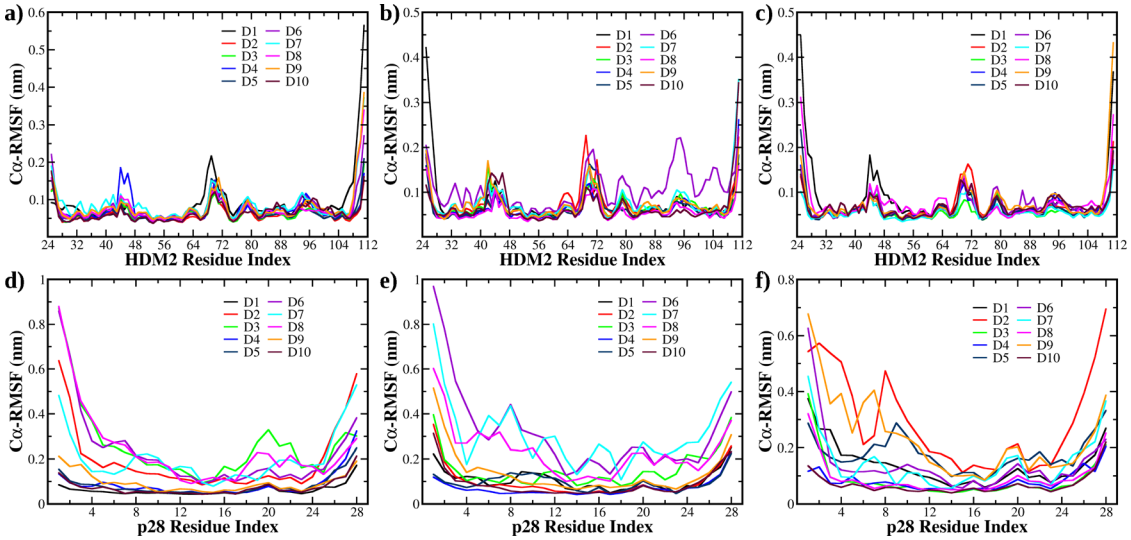

Fig. 6 Root mean square fluctuations (RMSF) of Cα carbon atoms of (a)–(c) the HDM2 protein and (d) and (e) the p28 peptide, calculated for three sets of MD trajectories of each docked structure using the last 50 ns of data. The analysis indicates that the HDM2 protein is structurally rigid, while the p28 peptide is highly flexible, allowing it to adapt to favourable binding modes.

in-depth for their various aspects of binding characteristics. The final binding poses of the p28 peptide with HDM2 for the three different sets of trajectories are depicted in Fig. 7.

RMSD-based clustering of these three MD trajectories was performed using GROMACS built-in tools to evaluate the stability and reproducibility of the docked p28–HDM2 complexes. This approach allowed us to quantify the dominant binding modes across three independent replicas for each model and compare their relative occupancy and consistency.

For D3, cluster 1 occupancy ranged from 43.8% to 57.1% across replicas, indicating moderate consistency. D4 exhibited the highest reproducibility, with cluster 1 occupancy of 100%, 84.6%, and 86.1% across the three replicas, demonstrating a consistently dominant binding mode. For D5, cluster 1 occupancy was 96.7% and 91.8% in replicas 1 and 2, but dropped to 36.1% in replica 3. Nevertheless, the binding region remained close to the HDM2 active site. The observed differences across replicas are mainly due to slight variations in the secondary structure of p28. These results support D4 as the most reproducible and stable binding mode among the top poses. Representative structures from the dominant RMSD-based clusters for D3, D4, and D5 across all three replicas are shown in Fig. 8, illustrating that p28 consistently occupies the hotspot region of the HDM2 NTD (Table 2).

3.4 Contact frequency maps

For the three selected complexes (D3, D4, and D5), we calculated the contact frequency between interacting residues, which is depicted as a contact frequency map in Fig. 9. The contact frequency map represents the probability of contacts between residues of HDM2 and p28, using data from the last 50 ns of the MD trajectories. A contact between two residues is defined if the distance between any of their heavy atoms is less than 4.5 Å. These contact maps provide valuable insights into the residues that engage in favourable and sustained interactions between HDM2 and p28. Contact frequency maps are helpful for understanding protein–protein interactions, as they highlight key residues involved in stable binding interfaces. By analysing these maps, we identified crucial interaction hotspots between HDM2 and p28 and assessed how p28 modulates the binding region of HDM2, potentially impacting its interaction with other cell growth regulatory proteins such as p53. The high contact frequency regions suggest critical sites for the stabilization of the HDM2–p28 complex.

To compare the contacts between the p28 peptide and HDM2 with the native p53–HDM2 interactions, we also mapped the contact frequency of the p53–HDM2 binding interface using the last 10 ns trajectory of a 100 ns simulation of this complex at 300 K. The key residues that form the native HDM2–p53 interactions are predominantly hydrophobic, along with some other residues involved in hydrogen-bonding interactions. The region of the HDM2 N-terminal domain (NTD) involved in these native interactions includes key residues within the range of 54–67, as well as residues 50, 72, 93, 96, and 99. Important hydrophobic residue pairs include LEU54–TRP23, ILE61–PHE19, VAL93–LEU22, VAL93–TRP23, MET62–PHE19, ILE99–LEU26, LEU54–LEU26, ILE61–TRP23, and LEU57–TRP23, where the first residue is from HDM2 and the second from p53. In addition, residue pairs such as TYR67–SER15, GLN72–THR18, GLN72–GLN16, GLN72–SER15, MET62–GLN16, and GLU25–ASN29 are involved in hydrogen-bonding and polar interactions.

In the D3 docked complex, HDM2 residues 50, 51, 54–59, 62, 67–74, 93, 96–100 and many others formed stable interactions during the 300 ns simulation. The p28 peptide residues 3, 4, 7, 8–12, 15, 16, 19, and 23–26 are involved in blocking the hydrophobic pocket of HDM2 by interacting with the above HDM2 residues. Prominent hydrophobic residue pairs include

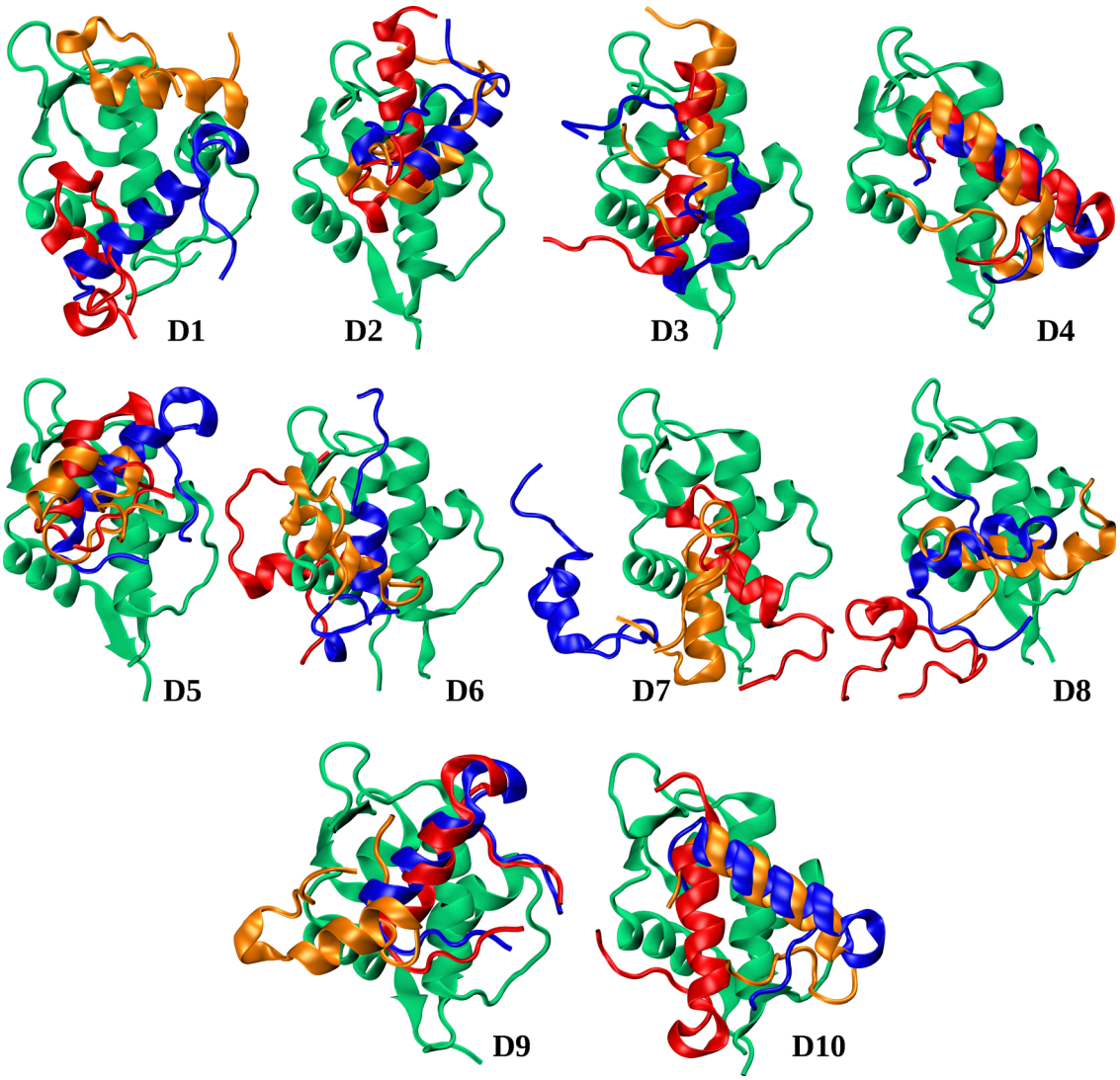

Fig. 7 Cartoon representation of the final binding poses of the p28 peptide with HDM2 after 300 ns of simulation for docked complexes D1 to D10. The HDM2 protein is coloured green, while the p28 peptide is shown in blue, red, and orange, with each colour depicting the binding pattern in three different trajectories.

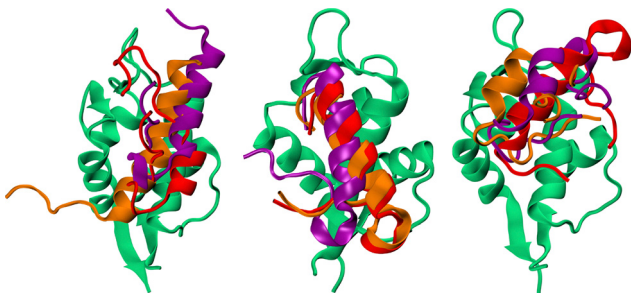

Fig. 8 Representative structures from the first RMSD-based cluster for D3, D4, and D5 across all three replicas. The results show that the p28 peptide predominantly occupies the hotspot region of the HDM2 N-terminal domain (NTD). The HDM2 NTD is shown in green, while the p28 peptide is depicted in red, orange, and purple to represent the different replicas.

Table 2 Percentage population of the dominant clusters from the RMSD-based clustering for protein models D3, D4, and D5 across three independent replicas

Replica	1	2	3
D3			
Cluster 1	43.76	57.05	52.21
Cluster 2	15.88	0.066	2.300
Cluster 3	14.21	0.041	2.175
D4			
Cluster 1	100.00	84.61	86.06
Cluster 2	0.0	1.545	1.97
Cluster 3	0.0	1.310	1.87
D5			
Cluster 1	96.69	91.78	36.12
Cluster 2	0.022	1.37	12.24
Cluster 3	0.010	0.985	12.21

TYR100–TYR23, MET62–ALA4, LEU54–MET15, LEU54–VAL11, MET50–LEU19, ILE99–MET15, TYR67–ALA4, TYR100–LEU19, VAL93–VAL11, VAL93–VAL10, and MET62–MET7. Additionally, other significant interactions were observed between residue

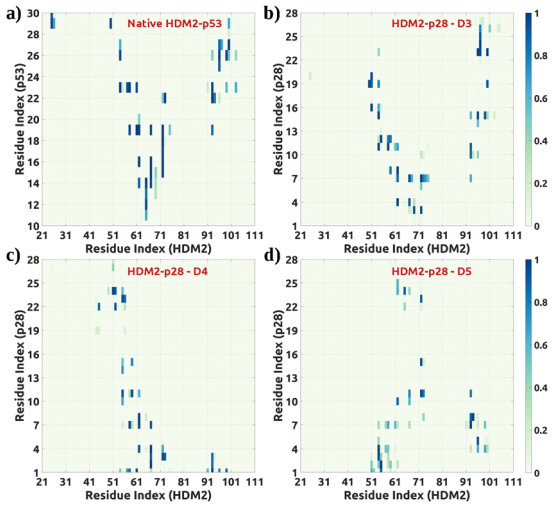

Fig. 9 (a) Contact frequency map of the native interaction between HDM2 and p53 residues. Contact frequency map of the HDM2–p28 interactions for (b) complex D3, (c) complex D4 and (d) complex D5. The map highlights prominent and sustained interactions between HDM2 and p53 residues, revealing key interaction points that inhibit the functional activity of p53.

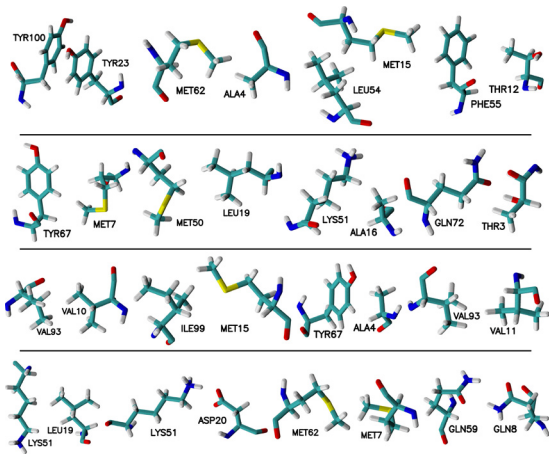

Fig. 10 Stick model representation of amino acid pairs forming prominent interactions between HDM2 and the p28 peptide in complex D3.

pairs GLN72–MET7, PHE55–THR12, TYR67–MET7, ARG97–LEU24, LYS51–ASP20, GLU69–THR3, ARG97–LYS25, and LYS51–LEU19. Fig. 10 depicts the amino acid pairs involved in stable interactions between HDM2 and the p28 peptide in the D3 complex.

In the D4 docked complex, HDM2 residues 51, 52, 55–62, 67, 73, 93, and many others formed stable interactions during the 300 ns simulation. The p28 peptide residues in the sequence range of 1–4, 7–11, and 22–23 are involved in masking the hydrophobic pocket of HDM2 by interacting with the above HDM2 residues. Important hydrophobic residue pairs include TYR67–ALA4, VAL93–LEU1, MET62–MET7, PHE55–TYR23, ILE61–LEU1, PHE55–VAL11, TYR67–MET7, and MET62–ALA4. Additionally, other notable interactions were observed between residue pairs TYR67–SER2, MET62–GLN8, GLN59–VAL11,

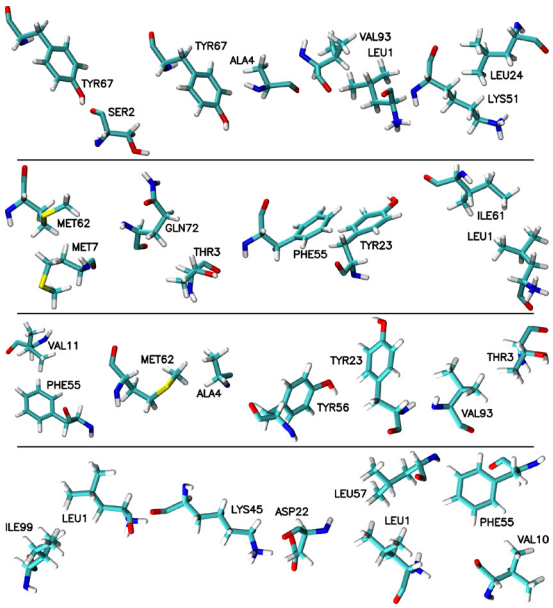

Fig. 11 Stick model representation of amino acid pairs forming prominent interactions between HDM2 and the p28 peptide in complex D4.

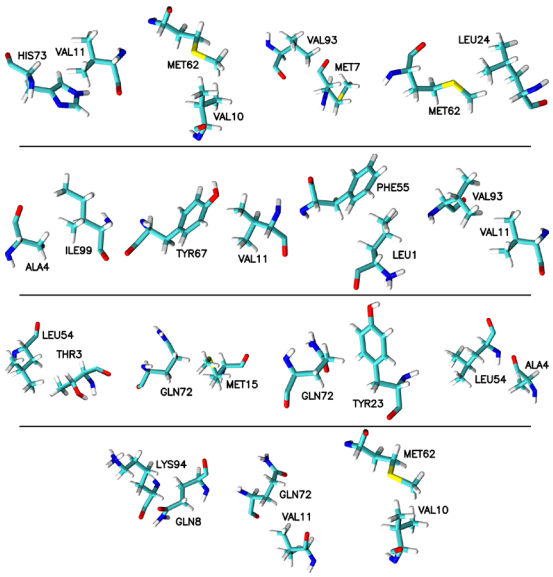

Fig. 12 Stick model representation of amino acid pairs forming prominent interactions between HDM2 and the p28 peptide in complex D5.

LYS51–LEU24, GLN72–THR3, GLU52–LEU24, GLU52–ASP22, TYR67–THR3, and HIS73–THR3. Fig. 11 depicts the amino acid pairs involved in stable interactions between HDM2 and the p28 peptide in the D4 complex.

In the D5 complex, the HDM2 residues at the binding interface were similar to those in the D4 complex. In the p28 peptide, residues 1–8, 10, 11, 15, 23, 24, and others were involved in crucial contacts. Important hydrophobic and polar interactions include PHE55–SER2, VAL93–MET7, LEU54–ALA4, LYS94–GLN8, GLN72–MET15, GLN72–TYR23, PHE55–LEU1, MET62–VAL10, VAL93–VAL11, and TYR67–VAL11. Fig. 12 illustrates the amino

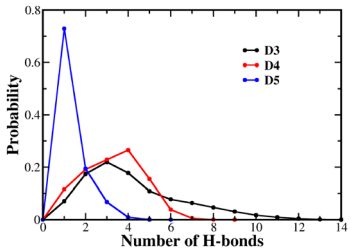

Fig. 13 Probability distribution of the number of hydrogen bonds (H-bonds) formed between the HDM2 NTD and the p28 peptide in complexes D3, D4, and D5.

acid pairs involved in the formation of prominent interactions within this complex.

In addition to the predominant hydrophobic interactions, we also analysed the conformations for hydrogen-bonding interactions, as they play crucial roles in stabilizing protein–protein interactions. Hydrogen bonds at protein interfaces often enhance the overall binding affinity and regulate the functional activity of proteins. We found that in the D3 complex, sustained hydrogen bonds are formed between the residue pairs 97ARG–24LEU, 51LYS–20ASP, 69GLU–2SER, 69GLU–3THR, and 72GLN–4ALA. In the D4 complex, hydrogen bonds are observed between the residue pairs 67TYR–2SER, 72GLN–4ALA, 45LYS–22ASP, 93VAL–1LEU, and 96HIS–1LEU. Similarly, in the D5 complex, residue pairs 65ARG–22ASP and 73HIS–12THR are involved in hydrogen bonding. We depict the probability distribution of H-bonds in each of these complexes in Fig. 13.

3.5 Binding energetics

Furthermore, the molecular mechanics Poisson–Boltzmann surface area (MMPBSA) method was employed to evaluate the binding energetics of the HDM2–p28 docked complexes.[42] This analysis was conducted using the gmxMMPBSA package.[43,44] MMPBSA is a widely used approach to estimate binding free energies by combining molecular mechanics (MM) energy terms with solvation energies calculated *via* the Poisson–Boltzmann (PB) equation and surface area (SA) contributions.

The binding free energy $\Delta G_{\text{binding}}$ was computed as the difference between the free energies of the complex, the receptor (HDM2), and the ligand (p28 peptide) as described in eqn (2). The total binding energy is derived from the sum of van der Waals, electrostatic, polar solvation, and non-polar solvation components, providing insights into the energetic contributions stabilizing the complexes. The calculations were based on snapshots extracted from the 300 ns molecular dynamics trajectories to capture representative conformations and interactions in each of the docked complexes.

$$\Delta G_{\text{bind}} = (E_{\text{complex}} - E_{\text{receptor}} - E_{\text{ligand}}) + (\Delta G_{\text{polar}} + \Delta G_{\text{nonpolar}}) \quad (2)$$

For the D3 complex, the MMPBSA binding energy was obtained to be -44.68 ± 5.48 kcal mol^{-1}, and for the D4 and D5 complexes, it was found to be -37.3 ± 7.87 kcal mol^{-1} and -41.92 ± 4.49 kcal mol^{-1}, respectively. These highly negative interaction energies indicate a strong affinity of the p28 peptide for the hydrophobic pocket of the HDM2 NTD, potentially hindering its association with the p53 protein. The consistency of the binding energies across the complexes suggests that the p28 peptide consistently stabilises its interaction with HDM2, thereby potentially disrupting the normal binding of HDM2 to its native substrates. This analysis helped quantify the energetic favourability of the different binding modes observed in the D3, D4, and D5 complexes.

3.6 Docking of HDM2, p28 and p53 TAD protein chains

Furthermore, we explored these different configurations to understand how they interact with the p53 TAD by performing a second docking of the HDM2–p28 complex with the p53 TAD. From the docked cluster structures, we observed that due to the presence of the p28 peptide at the HDM2 binding pocket, HDM2 is unable to interact with p53, making only limited contacts between the p53 TAD and its own other solvent-exposed regions. We depict snapshots of the best models

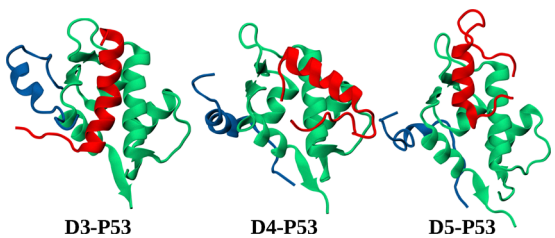

Fig. 14 Structures of the three relevant complexes from the 300 ns equilibrium MD run docked further with the p53 TAD, labelled as D3–P53, D4–P53, and D5–P53. These structures indicate that, in the presence of the p28 peptide, HDM2 is unable to interact with the p53 TAD. The HDM2 N-terminal domain (NTD) is coloured green, the p28 peptide is shown in red, and the p53 transactivation domain (TAD) is depicted in blue.

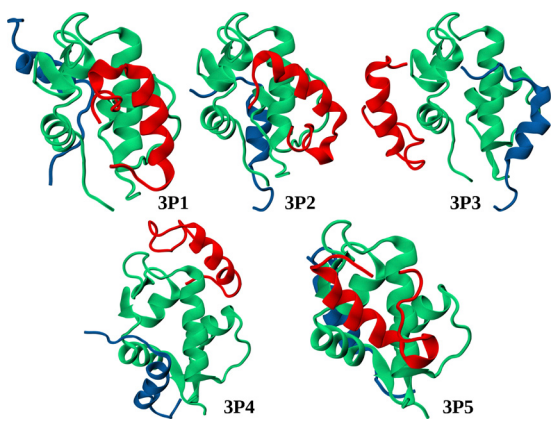

Fig. 15 First five structures obtained from the docking of the three protein chains – HDM2, p28, and p53 TAD, labelled as 3P1, 3P2, 3P3, 3P4 and 3P5. The structures show that p28 preferentially binds to the HDM2 hydrophobic pocket, preventing HDM2 from interacting with the p53 protein. The HDM2 N-terminal domain (NTD) is coloured green, the p28 peptide is shown in red, and the p53 transactivation domain (TAD) is depicted in blue.

obtained from this docking, labelled as D3–P53, D4–P53, and D5–P53, in Fig. 14. This highlights the efficacy of the p28 peptide in preserving the transcriptional activity of the p53 protein. In addition, we performed another docking of these with all three protein chains simultaneously. The results from the top clusters, scored by HADDOCK, revealed that the p28 peptide consistently binds to the hydrophobic pocket of HDM2, thereby preventing HDM2 from binding to the p53 TAD. The top 5 structures from this docking of the three protein chains, labelled as 3P1, 3P2, 3P3, 3P4 and 3P5, are shown in Fig. 15.

4 Cross-validation of docking poses

To further validate the docking results and minimize engine-specific bias, we performed additional docking of the p28–HDM2 complex using ClusPro and HDOCK. In ClusPro, the top-ranked poses consistently positioned p28 at the HDM2 hotspot region, in agreement with the HADDOCK-derived interface. In HDOCK, out of the top 10 models, the highest-scoring model, along with five others, placed p28 largely overlapping with the binding face, whereas the remaining models were positioned slightly away from the interface. These findings indicate that the hotspot-binding mode of p28 is reproducible across different docking platforms. The representative top-ranked models from ClusPro and HDOCK are depicted in Fig. 16.

5 Limitations of the study

This study is based entirely on computational modelling. The docking–MD workflow used here identifies plausible binding modes but does not capture spontaneous recognition or binding/unbinding pathways. Enhanced sampling methods and more rigorous free-energy calculations will be required to quantify binding thermodynamics and kinetics. The MMPBSA results are interpreted qualitatively, as they neglect entropy and dielectric sensitivity. The proposed competition between p28 and p53 for the HDM2 pocket is based on docking and steric overlap, not on alchemical competition or multi-ligand free-energy methods. Finally, our findings have not yet been validated against existing *in vitro* or *in vivo* data, such as affinity measurements or functional assays of p28, which remain essential for establishing the therapeutic relevance of the proposed mechanism.

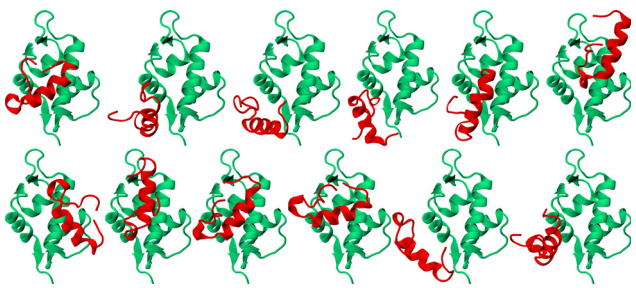

Fig. 16 Top six representative docking poses of the p28–HDM2 complex obtained from ClusPro (top panel) and HDOCK (bottom panel). The HDM2 N-terminal domain (NTD) is coloured green, and the p28 peptide is shown in red.

6 Conclusions

This study aimed to explore the potential mechanism by which the azurin-derived peptide p28 may contribute to tumour suppression, focusing on its interactions with the cancer-related protein HDM2. Using docking and multi-replica molecular dynamics (MD) simulations, we examined different binding possibilities of p28 to the HDM2 N-terminal domain (NTD).

Our results suggest that several HDM2–p28 complexes converge toward stable low-energy binding modes. Among these, three poses (D3, D4, and D5) consistently maintained interchain interactions and partially blocked the hydrophobic pocket of HDM2, including residues 54–72 and 93–99 that are critical for p53 binding. Interaction energy analysis using MMPBSA supported the relative stability of these complexes, although these values are interpreted as qualitative rankings rather than absolute binding free energies.

Secondary docking experiments with the p53 TAD indicated that, in the presence of p28, the canonical p53 binding interface of HDM2 is sterically hindered, suggesting a plausible mechanism by which p28 may interfere with HDM2–p53 association. While these findings are consistent with the proposed tumour-suppressive role of p28, we emphasize that they represent a computational hypothesis. Further validation using enhanced sampling, free-energy calculations, and experimental studies will be necessary to rigorously establish competitive binding and therapeutic relevance.

Overall, this work provides computational evidence supporting the plausibility of p28 as a modulator of the HDM2–p53 interaction and offers structural insights that may reveal the design of peptide-based anticancer strategies.

Conflicts of interest

The authors declare no competing interests.

Data availability

All relevant data are included in the article, and the structure, topology and parameter files of the docked HADDOCK complexes are available in the figshare repository: **https://figshare.com/s/55492629a8b293271593**. The scripts used for the analysis of the MD trajectory are also available, which include Python scripts to calculate the contact frequency between different residues of HDM2 and the p28 peptide and MATLAB scripts to create the contact frequency maps.

Supplementary information (SI) is available. See DOI: **https://doi.org/10.1039/d5cp02358k**.

Acknowledgements

RB acknowledges the Indian Institute of Technology Tirupati for its support through the new faculty seed grant (NFSG). A. J. and R. B. acknowledge the Indian Institute of Technology Tirupati for the computational facilities. R. B. acknowledges ANRF (SERB)-DST for funding through other projects (CRG/2021/003859 and EEQ/2021/000182) that helped to build part of the essential computational facilities used for the present work. R. B. acknowledges the National Supercomputing Mission (NSM) for providing computing resources of 'PARAM Seva at IIT Hyderabad, implemented by C-DAC and supported by the Ministry of Electronics and Information Technology (MeitY) and Department of Science and Technology (DST), Government of India. R. B. further acknowledges IIT Madras for partial computational support *via* the AQUA HPC facility.

References

1 L. Cahilly-Snyder, T. Yang-Feng, U. Francke and D. L. George, *Somatic Cell Mol. Genet.*, 1987, **13**, 235–244.
2 A. J. Levine, *Cell*, 1997, **88**, 323–331.
3 L. Wu and A. J. Levine, *Mol. Med.*, 1997, **3**, 441–451.
4 J. Momand, G. P. Zambetti, D. C. Olson, D. George and A. J. Levine, *Cell*, 1992, **69**, 1237–1245.
5 K. H. Vousden and X. Lu, *Nat. Rev. Cancer*, 2002, **2**, 594–604.
6 P. H. Kussie, S. Gorina, V. Marechal, B. Elenbaas, J. Moreau, A. J. Levine and N. P. Pavletich, *Science*, 1996, **274**, 948–953.
7 V. M. Jiandong Chen and A. J. Levine, *Mol. Cell. Biol.*, 1993, **13**, 4107–4114.
8 V. Böttger, A. Böttger, S. F. Howard, S. M. Picksley, P. Chène, C. Garcia-Echeverria, H. K. Hochkeppel and D. P. Lane, *Oncogene*, 1996, **13**, 2141–2147.
9 A. Böttger, V. Böttger, C. Garcia-Echeverria, P. Chène, H.-K. Hochkeppel, W. Sampson, K. Ang, S. F. Howard, S. M. Picksley and D. P. Lane, *J. Mol. Biol.*, 1997, **269**, 744–756.
10 J. D. Oliner, J. A. Pietenpol, S. Thiagalingam, J. Gyuris, K. W. Kinzler and B. Vogelstein, *Nature*, 1993, **362**, 857–860.
11 D. A. Freedman, C. B. Epstein, J. C. Roth and A. J. Levine, *Mol. Med.*, 1997, **3**, 248–259.
12 Z. Lai, K. R. Auger, C. M. Manubay and R. A. Copeland, *Arch. Biochem. Biophys.*, 2000, **381**, 278–284.
13 K. Sakaguchi, S. Saito, Y. Higashimoto, S. Roy, C. W. Anderson and E. Appella, *J. Biol. Chem.*, 2000, **275**, 9278–9283.
14 O. Schon, A. Friedler, M. Bycroft, S. M. Freund and A. R. Fersht, *J. Mol. Biol.*, 2002, **323**, 491–501.
15 Y. Haupt, R. Maya, A. Kazaz and M. Oren, *Nature*, 1997, **387**, 296–299.
16 M. H. G. Kubbutat and K. H. Vousden, *Mol. Cell. Biol.*, 1997, **17**, 460–468.
17 Y. Barak, T. Juven, R. Haffner and M. Oren, *EMBO J.*, 1993, **12**, 461–468.
18 S. M. Picksley and D. P. Lane, *BioEssays*, 1993, **15**, 689–690.
19 J. Wang, S. Lisanza, D. Juergens, D. Tischer, J. L. Watson, K. M. Castro, R. Ragotte, A. Saragovi, L. F. Milles, M. Baek, I. Anishchenko, W. Yang, D. R. Hicks, M. Expòsit, T. Schlichthaerle, J.-H. Chun, J. Dauparas, N. Bennett, B. I. M. Wicky, A. Muenks, F. DiMaio, B. Correia, S. Ovchinnikov and D. Baker, *Science*, 2022, **377**, 387–394.
20 J. L. Watson, D. Juergens, N. R. Bennett, B. L. Trippe, J. Yim, H. E. Eisenach, W. Ahern, A. J. Borst, R. J. Ragotte, L. F. Milles, B. I. M. Wicky, N. Hanikel, S. J. Pellock, A. Courbet, W. Sheffler, J. Wang, P. Venkatesh, I. Sappington, S. V. Torres, A. Lauko, V. De Bortoli, E. Mathieu, S. Ovchinnikov, R. Barzilay, T. S. Jaakkola, F. DiMaio, M. Baek and D. Baker, *Nature*, 2023, **620**, 1089–1100.
21 V. De Grandis, A. R. Bizzarri and S. Cannistraro, *J. Mol. Recognit.*, 2007, **20**, 215–226.
22 A. Yaghoubi, M. Khazaei, A. Avan, S. M. Hasanian, W. C. Cho and S. Soleimanpour, *Front. Oncol.*, 2020, **10**, 1–10.
23 F. Huang, Q. Shu, Z. Qin, J. Tian, Z. Su, Y. Huang and M. Gao, *Protein J.*, 2020, **39**, 182–189.
24 B. N. Taylor, R. R. Mehta, T. Yamada, F. Lekmine, K. Christov, A. M. Chakrabarty, A. Green, L. Bratescu, A. Shilkaitis, C. W. Beattie and T. K. Das Gupta, *Cancer Res.*, 2009, **69**, 537–546.
25 T. Yamada, T. K. Das Gupta and C. W. Beattie, *Mol. Pharmaceutics*, 2013, **10**, 3375–3383.
26 S. Santini, A. R. Bizzarri and S. Cannistraro, *J. Mol. Recognit.*, 2011, **24**, 1043–1055.
27 S. Signorelli, S. Santini, T. Yamada, A. R. Bizzarri, C. W. Beattie and S. Cannistraro, *Biochim. Biophys. Acta, Gen. Subj.*, 2017, **1861**, 910–921.
28 A. R. Bizzarri, I. Moscetti and S. Cannistraro, *Biochim. Biophys. Acta, Gen. Subj.*, 2019, **1863**, 342–350.
29 J. Hu, W. Jiang, J. Zuo, D. Shi, X. Chen, X. Yang, W. Zhang, L. Ma, Z. Liu and Q. Xing, *Commun. Biol.*, 2023, **6**, 59.
30 F. Domenici, M. Frasconi, F. Mazzei, G. D'Orazi, A. R. Bizzarri and S. Cannistraro, *J. Mol. Recognit.*, 2011, **24**, 707–714.
31 J. Kallen, A. Izaac, S. Chau, E. Wirth, J. Schoepfer, R. Mah, A. Schlapbach, S. Stutz, A. Vaupel, V. Guagnano, K. Masuya, T.-M. Stachyra, B. Salem, P. Chene, F. Gessier, P. Holzer and P. Furet, *ChemMedChem*, 2019, **14**, 1305–1314.
32 H. Nar, A. Messerschmidt, R. Huber, M. van de Kamp and G. W. Canters, *J. Mol. Biol.*, 1991, **221**, 765–772.
33 R. V. Honorato, P. I. Koukos, B. Jiménez-García, A. Tsaregorodtsev, M. Verlato, A. Giachetti, A. Rosato and A. M. J. J. Bonvin, *Front. Mol. Biosci.*, 2021, **8**, 729513.
34 R. V. Honorato, M. E. Trellet, B. Jiménez-García, J. J. Schaarschmidt, M. Giulini, V. Reys, P. I. Koukos, J. P. G. L. M. Rodrigues, E. Karaca, G. C. P. van Zundert, J. Roel-Touris, C. W. van Noort, Z. Jandová, A. S. J. Melquiond and A. M. J. J. Bonvin, *Nat. Protoc.*, 2024, **19**, 3219–3241.
35 M. J. Abraham, T. Murtola, R. Schulz, S. Páll, J. C. Smith, B. Hess and E. Lindahl, *SoftwareX*, 2015, **1**, 19–25.
36 S. Nosé, *Mol. Phys.*, 1984, **52**, 255–268.
37 W. G. Hoover, *Phys. Rev. A:At., Mol., Opt. Phys.*, 1985, **31**, 1695–1697.

38 M. Parrinello and A. Rahman, *J. Appl. Phys.*, 1981, **52**, 7182–7190.
39 S. Nosé and M. Klein, *Mol. Phys.*, 1983, **50**, 1055–1076.
40 T. Darden, D. York and L. Pedersen, *J. Chem. Phys.*, 1993, **98**, 10089–10092.
41 B. Hess, H. Bekker, H. J. C. Berendsen and J. G. E. M. Fraaije, *J. Comput. Chem.*, 1997, **18**, 1463–1472.
42 S. Genheden and U. Ryde, *Expert Opin. Drug Discovery*, 2015, **10**, 449–461.
43 B. R. R. Miller, T. D. J. McGee, J. M. Swails, N. Homeyer, H. Gohlke and A. E. Roitberg, *J. Chem. Theory Comput.*, 2012, **8**, 3314–3321.
44 M. S. Valdés-Tresanco, M. E. Valdés-Tresanco, P. A. Valiente and E. Moreno, *J. Chem. Theory Comput.*, 2021, **17**, 6281–6291.

